

# Reverse Shock Emission as a Probe of GRB Ejecta

E. McMahon,<sup>1</sup> P. Kumar<sup>1</sup> and T. Piran<sup>2,3</sup>

<sup>1</sup>*Department of Astronomy, University of Texas, Austin, TX 78712, USA*

<sup>2</sup>*Racah Institute for Physics, The Hebrew University, Jerusalem, 91904, Israel*

<sup>3</sup>*Theoretical Astrophysics, Caltech, Pasadena, CA 91125, USA*

5 February 2008

## ABSTRACT

We calculate the reverse shock (RS) synchrotron emission in the optical and the radio wavelength bands from electron-positron pair enriched gamma-ray burst ejecta with the goal of determining the pair content of GRBs using early time observations. We take into account an extensive number of physical effects that influence radiation from the reverse-shock heated GRB ejecta. We find that optical/IR flux depends very weakly on the number of pairs in the ejecta, and there is no unique signature of ejecta pair enrichment if observations are confined to a single wavelength band. It may be possible to determine if the number of pairs per proton in the ejecta is  $\gtrsim 100$  by using observations in optical and radio bands; the ratio of flux in the optical and radio at the peak of each respective reverse-shock light curve is dependent on the number of pairs per proton. We also find that over a large parameter space, RS emission is expected to be very weak; GRB 990123 seems to have been an exceptional burst in that only a very small fraction of the parameter space produces optical flashes this bright. Also, it is often the case that the optical flux from the forward shock is brighter than the reverse shock flux at deceleration. This could be another possible reason for the paucity of prompt optical flashes with a rapidly declining light curve at early times as was seen in 990123 and 021211. Some of these results are a generalization of similar results reported in Nakar & Piran (2004).

**Key words:** gamma-rays: bursts, theory, methods: analytical – radiation mechanisms: non-thermal - shock waves

## 1 INTRODUCTION

Since the discovery of the bright optical flash from GRB 990123 (Akerlof et al. 1999), many authors have considered this early afterglow emission as being due to the reverse shock passing through baryonic ejecta from the explosion, as was predicted by Sari & Piran (1999). If this early emission is indeed caused by the reverse shock (hereafter RS) passing through the ejecta, then this emission provides direct information about the composition and magnetic field strength and orientation in the material ejected from the inner engine, giving us clues about the nature of the outflow and the inner engine itself. Early optical afterglow data from GRBs 990123 & 021211 have already been used to infer that the ejecta from these GRBs may have been fairly highly magnetized baryonic ejecta (Zhang et al. 2003; Fan et al. 2002; Kumar & Panaitescu 2003; McMahon et al. 2004).

Only the observations of GRBs 990123 & 021211 have exhibited this steeply falling off early optical emission, while other bursts observed in the optical so quickly following the burst have exhibited either rising emission (030418), shallower fall-off (021004), or no emission at

all (Kehoe et al. 2001). There have also been some *Swift*-detected bursts recently that have not exhibited the steeply falling off emission expected from the RS (e.g. GRB 050319; Rykoff, Schaefer, & Quimby 2005) or optical/IR emission varying on very short timescales, seemingly following the activity of the central engine (GRB 041219a; Blake et al. 2005; Vestrand et al. 2005)<sup>1</sup>. There have also been some early optical upper limits from *Swift* of  $V \sim 21$  magnitude within minutes after the burst (e.g. 050219a; Schady et al. 2005). This lack of observations of the optical flash begs the question: are GRBs 990123 and 021211 unique? What is the reason for the lack of optical flashes? These early upper limits on RS emission can provide information about the ejecta and help to answer these questions.

In our previous paper (McMahon et al. 2004, hereafter MKP04), we estimated the RS emission and break frequencies at deceleration for a baryonic outflow for 10 bursts with

<sup>1</sup> Note however, that the situation in GRB 041219a is not clear as the correlation reported in Vestrand et al. (2005) should have been enhanced with a further temporal division of the optical signal.

burst parameters determined from afterglow modeling (assuming deceleration time is on the order of the burst duration, as occurs in 990123). We determined that a possible reason for weak RS optical emission after deceleration for most bursts is due to a cooling frequency below the optical band at deceleration. Although the reverse shock emission is expected to be bright ( $R$ -mag  $\sim 10$ ) at deceleration, when the cooling frequency drops below the observing band, no more emission from the ejecta is observed, with the exception of off-axis emission which falls off very quickly, as  $\sim 1/t^{(2+p/2)} \sim 1/t^3$  (Kumar & Panaitescu 2000). However, now that it is possible to quickly follow up GRBs with *Swift* UVOT, we are not seeing any bright optical flashes with this  $1/t^3$  falloff. This suggests that the RS flux is suppressed for some reason.

In the calculation in MKP04, we assumed the ejecta was purely baryonic. This may not be the case. If many  $e^\pm$  pairs are present in the ejecta (mixed with baryons), either ejected from the source or created by dissipation during the GRB, or if the magnetic field strength in the ejecta is very large (perhaps because the outflow was Poynting flux dominated), the RS emission could be suppressed significantly from the baryon dominated picture. Pair-enrichment of the ejecta causes reverse shock emission to be fainter than that expected from completely baryonic ejecta, and a very high ejecta magnetic field is likely to weaken the reverse shock as well; both scenarios provide alternate possibilities for suppression of reverse shock emission. It is useful then to determine the defining characteristics of reverse shock light curves and spectra for a baryonic, lepton-enriched, or highly magnetized ejecta, in order to distinguish between these possibilities when the *Swift* satellite and other robotic telescopes accumulate more multi-wavelength afterglow data at early times.

Pair enrichment of the ejecta has been looked at by Li et al. (2003) and the case of highly magnetized ejecta has been investigated by Zhang & Kobayashi (2005). In this paper, we take another look at pair-enrichment; we take into account that the reverse shock is mildly relativistic, and also carry out a self consistent cooling and self absorption calculation, which is necessary, since the ejecta self absorption frequency can be on the order of or greater than the cooling frequency. Li et al. (2003) predicted a bright IR flash with pair-enriched ejecta, as bright as that expected in the optical with strictly baryonic ejecta; we find that the optical/IR flux levels at deceleration have very little dependence on the number of pairs. Also, any change in spectral peak frequency or optical/IR flux at deceleration due to pair enrichment can also arise if the microphysics parameters in the ejecta are changed, thus creating a highly degenerate problem.

We first describe our model of reverse shock emission and the new physics we have added to the RS emission calculation (Section 2), then discuss our results (Section 3). In Section 4, we summarize the differences between baryonic and pair-enriched ejecta.

## 2 DESCRIPTION OF THE REVERSE SHOCK MODEL

Here, we briefly describe our RS model, then focus on the improvements we have made to the calculation of emission from the RS. For this calculation, we use the equations for the ejecta dynamics and RS emission described in Kumar & Panaitescu 2003 (KP03), Panaitescu & Kumar 2004 (PK04), and Nakar & Piran 2004 (NP04) and include synchrotron and inverse Compton cooling. We have added several new components to the calculation, namely (1) the effect of synchrotron & self inverse-Compton scattering on electron cooling & synchrotron self absorption frequencies, (2) inverse Compton cooling of RS electrons by synchrotron flux of the forward shock (hereafter FS), (3) absorption of RS photons (particularly in the radio band) in the FS region as they traverse through the FS on their way to the observer, and (4) pair-enriched ejecta.

### 2.1 The Standard Model: Dynamics & Synchrotron Emission in the RS

The ejecta dynamics are determined by assuming an initial Lorentz factor  $\Gamma_0$ , the burst duration in the observer frame  $t_{GRB}$ , number density of the external medium  $n_0 = AR^{-s}$  where  $R$  is the radial distance from the center of the explosion, and isotropic equivalent energy  $E_{52} = E/10^{52}$  ergs. The Lorentz factor of the shocked ejecta with respect to the unshocked external medium is given by (PK04)

$$\Gamma = \Gamma_0 \left(1 + 2\Gamma_0 (n_0/n_{ej})^{1/2}\right)^{-1/2} \quad (1)$$

where  $n_{ej} = E/(4\pi m_p c^2 R^2 \Gamma_0^2 \Delta)$  is the comoving ejecta density and  $\Delta$  is the lab frame ejecta width, taken to be  $ct_{dur} + R/(2\Gamma_0^2)$ , where  $t_{dur}$  is the host galaxy frame burst duration,  $t_{GRB}/(1+z)$ . When  $\Delta \sim ct_{dur}$  at deceleration, we define this case to be the non spreading ejecta case (also called thick ejecta), whereas when  $\Delta \sim R/(2\Gamma_0^2)$ , we define this case to be the spreading ejecta case (also called thin ejecta).

When  $\Gamma_0^2 n_0/n_{ej} \gg 1/4$  near shock crossing time (the time at which the RS reaches the rear of the ejecta shell), the RS is relativistic and the bulk Lorentz factor  $\Gamma \propto R^{(s-2)/4}$  and the ejecta radius  $R \propto t^{2/(4-s)}$  ( $t$  is time in the observer frame), prior to deceleration time, for the case of non-spreading ejecta. In the case of spreading ejecta,  $\Gamma_0^2 n_0/n_{ej} \sim 0.3$  for  $s = 0$  and  $\sim 0.5$  for  $s = 2$  at shock crossing time, so the RS is mildly relativistic. The radial distance of the ejecta from the center of the explosion at the time when the RS reaches the back of the ejecta shell (the shock crossing radius) is given in Table 1, as are the Lorentz factor and observer time at this radius. See Table 2 for the scalings of variables with observer time before deceleration, numerically determined for the mildly relativistic case.

The reverse shock speed with respect to the unshocked ejecta as measured in the lab frame is (KP03)

$$\beta_0 - \beta_{RS} = \frac{1.4}{\Gamma_0^2} \left( \frac{\Gamma_0^2 n_0}{n_{ej}} \right)^{1/2} \quad (2)$$

where  $\beta_{RS}$  is the reverse shock speed measured in the lab frame and  $\beta_0$  is the outflow speed measured in the lab frame as well. The above equation is valid in all cases, from non-

relativistic to relativistic RS cases. It can be shown (PK04) that the radius at which the reverse shock has traversed the ejecta is within a factor of  $\sim 2$  of the deceleration radius for both a wind and homogeneous external medium.

The rate at which the ejecta electrons are swept up by the RS is given by

$$\frac{dN_e}{dR} = \frac{1.4}{\Gamma_0} \left( \frac{n_0}{n_{ej}} \right)^{1/2} \frac{N_p}{\Delta} \quad (3)$$

where  $N_p = E/(\Gamma_0 m_p c^2)$  is the total number of protons in the ejecta. For spreading ejecta,  $N_e(R) \propto R^{3/2}$  for  $s = 0$  and  $R^{0.68}$  for  $s = 2$  (determined numerically) and for ejecta whose width is dominated by the GRB duration  $N_e(R) \propto R^{(4-s)/2}$ .

After deceleration (shock crossing time), the ejecta bulk Lorentz factor is assumed to evolve adiabatically following the Blandford-McKee solution, as described in PK04, as

$$\Gamma_{ej} \propto R^{-(3-s)/2} (R^{(2a-3)} \Delta'^a)^{-1.5(4-s)/(17-4s)}. \quad (4)$$

where  $a$  is the adiabatic index, set to  $4/3$  for relativistic ejecta and  $5/3$  for non-relativistic ejecta, and  $\Delta' = \max(\Gamma_{ej} c t_{dur}, R/2\Gamma_{ej})$  is the comoving frame ejecta width. We take the ejecta expansion in the radial direction to be relativistic when the minimum electron thermal Lorentz factor in the ejecta  $\gtrsim 10$ , and nonrelativistic when it is  $< 10$ .

Synchrotron radiation from the shocked electrons is calculated assuming a power law distribution of electron energy with index  $p$ , i.e.  $dN_e/d\gamma \propto \gamma^{-p}$  for  $\gamma > \gamma_{ir}$  (where  $\gamma_{ir}$  is the minimum electron thermal Lorentz factor averaged over all of the electrons as they cross the RS front),  $\varepsilon_{Br}$ , the fraction of energy in the magnetic field, and  $\varepsilon'_e$ , the minimum thermal energy given to the electrons;  $\gamma_{ir} = \varepsilon'_e \langle e_p \rangle / m_e c^2$ , where  $e_p = m_p c^2 (\Gamma' - 1)$  is the minimum thermal energy per proton just behind the RS front,  $\langle e_p \rangle \sim 0.5 e_p$ , and

$$\Gamma' = \Gamma_0 \Gamma (1 - \beta_0 \beta) \simeq 0.5 \left( \frac{\Gamma}{\Gamma_0} + \frac{\Gamma_0}{\Gamma} \right) \quad (5)$$

is the relative Lorentz factor of the shocked and unshocked ejecta. Since  $\Gamma' \lesssim 2$ , we cannot approximate the evolution of  $\gamma_{ir}$  by assuming  $\gamma_{ir} \propto \Gamma'$ ; we numerically calculate the evolution for radii near the shock crossing radius, the results given in Table 2. The comoving magnetic field strength in the ejecta is given by  $B' = [8\pi \varepsilon_{Br} n_{ej} \langle e_p \rangle (4\Gamma' + 3)]^{1/2}$ .

We note that  $\gamma_{ir}$  can be less than 1, since  $\gamma_{ir} m_e c^2$  is defined to be the minimum thermal energy for electrons. We take into account that some fraction of the electrons are nonrelativistic and emit cyclotron radiation. We remove these electrons from the electron column density used for our synchrotron calculation, i.e.  $n_{col,r} = N_e(\gamma_{ir})^{p-1}/4\pi R^2$ , and set the minimum thermal energy for electrons to be  $m_e c^2$ .

After deceleration, for adiabatically cooling electrons,  $\gamma_{ir} \propto V'^{-(a_e-1)} \propto (R^2 \Delta')^{-1/3}$ , where  $V'$  is the comoving ejecta volume, and the ratio of specific heats is  $a_e = 4/3$ . The magnetic field is assumed to be predominantly transverse and frozen into the ejecta, decaying as  $B' \propto (R \Delta')^{-1}$ . When radiative cooling becomes less important than adiabatic cooling, the Lorentz factor of electrons cooling on a dynamical timescale,  $\gamma_{cr}$  (discussed in more detail below), evolves in the same manner as  $\gamma_{ir}$ .

The observer frame synchrotron injection frequency is calculated with

$$\nu_{ir} = \frac{0.98 q B' \gamma_{ir}^2 \Gamma}{2\pi m_e c (1+z)}, \quad (6)$$

where we use here and elsewhere the common notation of  $\nu_x$  being the synchrotron frequency of an electron with a Lorentz factor  $\gamma_x$ . The synchrotron flux at the peak of the  $f_\nu$  spectrum is given by

$$F_{pr} = \frac{N_e P_{\nu_p} \Gamma (1+z)}{4\pi d_L^2} \quad (7)$$

where  $N_e \equiv N_e(R)$  is the number of electrons heated by the RS determined from Equation 3,  $P_{\nu_p} = 1.04 q^3 B/m_e c^2$  is the comoving power radiated per electron per unit frequency at the peak of  $f_\nu$ , and  $d_L = 2c\sqrt{1+z}[(1+z)^{1/2} - 1]/H_0$  is the luminosity distance. We use  $H_0 = 65 \text{ km s}^{-1} \text{ Mpc}^{-1}$  and for simplicity  $\Omega = 1$ ,  $\Lambda = 0$ . The factors of 0.98 in Equation 6 and 1.04 above for  $P_{\nu_p}$  are from Wijers & Galama (1999) for the case of  $p = 2$ .

## 2.2 Inverse Compton Cooling & Synchrotron Self Absorption

We include the inverse Compton process to calculate electron cooling. The Compton  $Y$  parameter is obtained by solving the equation describing radiative loss of energy for a single electron with a Lorentz factor  $\gamma_e$

$$\frac{d(\gamma_e m_e c^2)}{dt'} = -\frac{\sigma_T c B'^2 \gamma_e^2 \beta_e^2}{6\pi} \times \left[ \frac{f'_{\nu' > \nu'_a}}{f'_{total}} + \frac{\tau_{es} \gamma_p^2 \beta_p^2}{\nu'_p \sigma_T} \int d\nu' \frac{f(\nu') \sigma_{KN}}{(1 + \tau_{sa}(\nu'))} \right] \quad (8)$$

where primes denote variables measured in the rest frame of the shocked fluid. The bracketed terms on the RHS are effectively  $(1 + Y)$ ; the first part, the fraction of energy emitted from one electron with Lorentz factor  $\gamma_e$  that is not absorbed by material in emitting region, is given by

$$\frac{f'_{\nu' > \nu'_a}}{f'_{total}} = \begin{cases} \frac{9x^{4/3} - 25.63}{5x^{4/3} - 25.63} & \text{for } \nu'_c > \nu'_a \\ \frac{3[2e^{-x}\sqrt{x} + \sqrt{\pi}(1 - \text{Erf}(\sqrt{x}))]}{e^{-x}(2x^{3/2} + 6\sqrt{x}) + 3\sqrt{\pi}(1 - \text{Erf}(\sqrt{x}))} & \text{for } \nu'_c < \nu'_a \end{cases} \quad (9)$$

where  $x = \nu'_a/\nu'_c$  and Erf is the error function. This equation is necessary for calculating electron cooling, since  $\nu'_c$  can be less than the self absorption frequency,  $\nu'_a$ , in the RS.

The second part of the bracketed term in Equation 8 is equivalent to  $Y$ ;  $\tau_{es}$  is the Thomson optical depth to electron scattering,  $\gamma_p = \min(\gamma_i, \gamma_e)$  and  $\beta_p$  is the corresponding velocity in units of  $c$ ,  $\nu'_p = \min(\nu'_i, \nu'_e)$ ,  $\sigma_{KN}$  is an approximation of the Klein-Nishina correction to the electron scattering cross section,  $\tau_{sa}(\nu')$  is the optical depth to synchrotron self absorption, and  $f(\nu')$  is the normalized set of broken power-laws describing the synchrotron spectrum (i.e.  $f(\nu'_p) = 1$ ).

Both of the bracketed terms of the effective  $(1 + Y)$  (Equation 8) are dependent on  $\nu'_c$  and  $\nu'_a$ , and in turn,  $\nu'_c$  is also dependent on  $(1 + Y)$ , so the equations for the three variables must be solved simultaneously; this has been done for all numerical results in this paper. It is, however, possible to semi-analytically estimate  $\nu'_c$  when we assume that  $Y \ll 1$

**Table 1.** Values of Parameters at Deceleration

	$\Delta = ct_{dur}$ $s = 0$	$\Delta = ct_{dur}$ $s = 2$	$\Delta = R_+/2\Gamma_0^2$ $s = 0$	$\Delta = R_+/2\Gamma_0^2$ $s = 2$
$R_+ =$	$\left[ \frac{16t_{dur}}{5.6^2\pi m_p c} \frac{E}{A} \right]^{1/4}$	$\left[ \frac{4t_{dur}}{5.6^2\pi m_p c} \frac{E}{A} \right]^{1/2}$	$\left[ \frac{9}{7.9^2\pi m_p c^2} \frac{E}{A\Gamma_0^2} \right]^{1/3}$	$\left[ \frac{1}{7.9^2\pi m_p c^2} \frac{E}{A\Gamma_0^2} \right]$
$\Gamma_+ =$	$0.55 \left( \frac{E}{n_0 m_p c^5 \pi t_{dur}^3} \right)^{1/8}$	$0.51 \left( \frac{E}{A m_p c^3 \pi t_{dur}} \right)^{1/4}$	$0.69\Gamma_0$	$0.83\Gamma_0$
$t_{obs,+} =$	$2.8t_{dur}$	$1.4t_{dur}$	$\left( \frac{1.1E}{n_0 c^5 m_p \pi \Gamma_0^8} \right)^{1/3}$	$\frac{0.02E}{A m_p c^3 \pi \Gamma_0^4}$
$\langle \epsilon_{p,+} \rangle =$	$\Gamma_0 \left( 0.18 n_0 m_p c^5 \pi t_{dur}^3 E^{-1} \right)^{1/8}$	$\Gamma_0 \left( 0.79 A m_p c^3 t_{dur} \pi E^{-1} \right)^{1/4}$	$0.03$	$0.01$
$\Gamma'_+ =$	$\left( 0.91 n_0 m_p c^5 \pi t_{dur}^3 \Gamma_0 E^{-1} \right)^{1/8}$	$\left( 0.99 A m_p c^3 \pi t_{dur} \Gamma_0 E^{-1} \right)^{1/4}$	$1.07$	$1.02$
$B'_+ = \epsilon_{Br,-1}^{1/2} \mathcal{L}_{ep}^{1/2} \times$	$21.5 \left( n_0^3 E_{52} t_{dur}^{-3} \right)^{1/8} \text{ G}$	$2.2 \times 10^4 \left( A_*^3 E_{52}^{-1} t_{dur}^{-3} \right)^{1/4} \text{ G}$	$4.1 n_0^{1/2} \Gamma_{0,2} \text{ G}$	$3.3 \times 10^5 A_*^{3/2} \Gamma_{0,2}^3 E_{52}^{-1} \text{ G}$
$F_{p,+} = \frac{\epsilon_{Br,-1}^{1/2} \mathcal{L}}{\mathcal{L}_{ep}^{1/2} (\sqrt{1+z}-1)^2} \times$	$791.0 n_0^{1/4} E_{52}^{5/4} t_{dur}^{-3/4} \Gamma_{0,2}^{-1} \text{ mJy}$	$1.3 \times 10^5 A_*^{1/2} E_{52} t_{dur}^{-1} \Gamma_{0,2}^{-1} \text{ mJy}$	$26.1 n_0^{1/2} E_{52} \Gamma_{0,2} \text{ mJy}$	$2.6 \times 10^6 A_*^{3/2} \Gamma_{0,2}^3 \text{ mJy}$
$\nu_{ir,+} = \frac{\epsilon_{Br,-1}^{1/2} \epsilon_{er,-1}^2 \mathcal{L}_{ep}^{5/2}}{\mathcal{L}^2 (1+z)} \times$	$5.1 \times 10^{11} n_0^{1/2} \Gamma_{0,2}^2 \text{ Hz}$	$5.4 \times 10^{16} A_* \Gamma_{0,2}^2 t_{dur}^{-1/2} E_{52}^{-1/2} \text{ Hz}$	$2.4 \times 10^{10} n_0^{1/2} \Gamma_{0,2}^2 \text{ Hz}$	$2.6 \times 10^{14} A_*^{3/2} \Gamma_{0,2}^4 E_{52}^{-1} \text{ Hz}$
$\nu_{cr,+} = \epsilon_{Br,-1}^{3/2} (1+z) \mathcal{L}_{ep}^{3/2} \times$	$1.6 \times 10^{17} n_0^{-1} E_{52}^{-1/2} t_{dur}^{-1/2} \text{ Hz}$	$3.6 \times 10^9 E_{52}^{1/2} t_{dur}^{1/2} A_*^{-2} \text{ Hz}$	$2.2 \times 10^{16} \Gamma_{0,2}^{4/3} A_*^{-5/6} E_{52}^{-2/3} \text{ Hz}$	$5.3 \times 10^8 E_{52} A_*^{-5/2} \Gamma_{0,2}^{-2} \text{ Hz}$
$f_{\nu,R} = \epsilon_{er,-1}^{1.5} \epsilon_{Br,-1}^{0.88} \mathcal{L}_{ep}^{1.38} \mathcal{L}^{-0.5} \times$	$12.9 n_0^{0.63} E_{52}^{1.3} \Gamma_{0,2}^{0.5} t_{dur}^{-3/4}$	$1.2 \times 10^7 A_*^{1.3} \Gamma_{0,2}^{0.63} t_{dur}^{-1.4}$	$0.043 n_0^{0.88} \Gamma_{0,2}^{2.5} E_{52}$	$4.6 \times 10^6 A_*^{2.6} \Gamma_{0,2}^6 E_{52}^{-0.75}$

$A_* = A/10^{35}$ ,  $E_{52} = E/10^{52}$ ,  $\Gamma_{0,2} = \Gamma_0/100$ ,  $\epsilon'_{er,-1} = \epsilon'_{er}/0.1$  and  $\epsilon_{Br,-1} = \epsilon_{Br}/0.1$ .  $f_{\nu,R}$  is the flux at deceleration in mJy in the R-band for  $p = 2.5$  and  $z = 1$ , for which  $(\nu_{ir}, \nu_{ar}) < \nu_R < \nu_{cr}$  is assumed. For full expression used in Figure 5, see Appendix A.

**Table 2.** Scalings Before Deceleration

	$\Delta = ct_{dur}$ $s = 0$	$\Delta = ct_{dur}$ $s = 2$	$\Delta = R_+/2\Gamma_0^2$ $s = 0$	$\Delta = R_+/2\Gamma_0^2$ $s = 2$
$R$	$t^{1/2}$	$t$	$t^{0.67}$	$t^{0.88}$
$\Gamma$	$t^{-1/4}$	$t^0$	$t^{-0.17}$	$t^{-0.066}$
$\gamma_{ir}$	$t^{0.45}$	$t^0$	$t^{1.7}$	$t^{0.62}$
$f_{\nu,X}$	$t^{-0.18+0.19p}$	$t^{1-0.5p}$	$t^{1.5(p-1)}$	$t^{0.012+0.082p}$
$f_{\nu,R}$	$t^{0.29+0.19p}$	$t^{-0.5(p-1)}$	$t^{-0.86+1.5p}$	$t^{-0.56+0.082p}$

Values of exponents in this table are determined numerically for mildly relativistic spreading ejecta and determined analytically for relativistic non spreading ejecta, near, but prior to, deceleration time.  $t$  is time measured in the observer frame. For the non-relativistic case of  $\Gamma_0^2 n_0/n_{ej} \ll 1/4$ ,  $\Gamma \propto R^0$  and  $R \propto t$ .  $f_{\nu,X}$  is the synchrotron flux for  $\nu_{obs} > (\nu_{ir}, \nu_{cr}, \nu_{ar})$ , and  $f_{\nu,R}$  is the synchrotron flux for  $(\nu_{ir}, \nu_{ar}) < \nu_{obs} < \nu_{cr}$ . Scalings after deceleration can be found in e.g. PK04. Note: it is possible for  $f_{\nu,X}$  to be decaying before deceleration because it peaks well before deceleration.

and IC does not contribute to the cooling calculation (see Table 1).

The comoving frame synchrotron self absorption frequency is calculated by equating the comoving synchrotron flux at  $\nu'_a$  to flux from a black body in the Rayleigh-Jeans part of the spectrum, or

$$2kT \frac{\nu_a'^2}{c^2} = f'_\nu(\nu'_a) \quad (10)$$

where  $kT = \max[\gamma_a, \min(\gamma_i, \gamma_c)] m_e c^2$ . A frequent arrangement of the RS break frequencies at deceleration is  $\nu'_i < \nu'_a < \nu'_c$ ; in this case,

$$\nu'_a = \left[ \frac{f'_p}{2m_e} \nu_i'^{\frac{(p-1)}{2}} \left( \frac{qB'}{2\pi m_e c} \right)^{1/2} \right]^{\frac{2}{(4+p)}} \quad (11)$$

where  $f'_p = N_e \sqrt{3} q^3 B' / (4\pi R^2 m_e c^2)$  is the comoving flux at the peak of  $f'_\nu$ .

The scalings of RS optical and X-ray flux with observer time just before deceleration for the four cases of  $s = 0, 2$  and  $\Delta = (ct_{dur}, R/2\Gamma_0^2)$  are shown in Table 2. Only synchrotron emission is included for these scalings (inverse Compton is also important in the X-ray), and  $Y \ll 1$  is assumed (the scaling for  $f_{\nu,R}$  is not affected, but  $f_{\nu,X}$  may be).

After deceleration, if ejecta is in the radiative regime, we continue to calculate the RS cooling and synchrotron self absorption frequencies  $\nu_{cr}$  and  $\nu_{ar}$  and the effective  $(1+Y)$  by solving Equations 8 & 10 simultaneously, as done before deceleration. If adiabatic cooling is more efficient,  $\gamma_{cr}$  decays as  $\gamma_{ir}$  (§ 2.1) and the self absorption frequency is solved for using Equation 10. After  $\nu_{cr}$  falls below the observing band, the ejecta emission turns off, and the observed flux is due to off axis emission that decays approximately as  $t^{-(4+p)/2}$  (Kumar & Panaitescu 2000).

### 2.3 Inverse Compton cooling by an external source

We have also allowed for external sources of flux to influence the cooling of electrons in the ejecta. In particular, we

include synchrotron flux from the FS incident on the ejecta in our calculation of  $\nu_{cr}$ . The external synchrotron flux in the shocked ejecta comoving frame is given by

$$f_{ex} = \frac{\tau_{es,ex} c B'_{ex}{}^2 \gamma_{e,ex}^2}{6\pi} \quad (12)$$

where the subscript “ $ex$ ” denotes values from a source external to the cooling calculation being done (here, FS flux is the external flux incident on the RS ejecta),  $\gamma_{e,ex}^2$  is the average electron thermal electron Lorentz factor squared in the forward shock. The equation for  $\gamma_c$  which includes the contribution of  $f_{ex}$  to the electron cooling is:

$$\gamma_c = \frac{1}{\chi_1 (1+Y) + \frac{\chi_2 f_{ex}}{\sigma_{KN,ex}}} \quad (13)$$

where  $\chi_1 = \sigma_T B'^2 t' / (6\pi m_e c^2)$ ,  $\chi_2 = \sigma_T t' / (m_e c^2)$ , and  $\sigma_{KN,ex} = [h\nu_{p,ex} \gamma_c / (m_e c^2)]^{1+\alpha_{ex}}$  is an approximation to the Klein-Nishina correction on the external flux, and  $\nu_{p,ex}$  is the peak of the  $\nu f_\nu$  spectrum in the FS;  $\alpha_{ex} = -0.5$  if  $\nu_{i,ex} > \nu_{c,ex}$ , and  $(1-p)/2$  if  $\nu_{i,ex} < \nu_{c,ex}$ . We also allow for FS synchrotron self-Compton flux to influence RS cooling; however the high energy ( $\gg m_e c^2$ ) of the FS synchrotron flux suppresses self-inverse Compton scattering, thus not significantly contributing to the RS cooling calculation. We do not consider the effect of RS emission on FS cooling; at most it is an order unity effect.

### 2.4 Absorption of RS Photons in the FS Material

We include the effect of absorption of RS photons in the FS material. For a selected observing band,  $\nu_{obs}$ , the optical depth to absorption is

$$\tau_{abs,FS} = \begin{cases} \left( \frac{\nu_{obs}}{\nu_{af}} \right)^{5/3} & \nu_{obs} < \min(\nu_{cf}, \nu_{if}) \\ \left( \frac{\nu_{obs}}{\nu_{af}} \right)^{-(p+4)/2} & \nu_{obs} > \min(\nu_{cf}, \nu_{if}) \end{cases} \quad (14)$$

where  $\nu_{af}$  is the observer frame FS synchrotron self absorption frequency. Before deceleration, the shocked ejecta and FS medium are moving together; however, after deceleration, these regions are moving at different Lorentz factors,

and one must take care to use the appropriate value of  $\nu_{af}$  when the RS photons are passing through the FS.

After calculating the RS emission as described above, the absorption in the FS is taken into account by reducing the RS flux by a factor of  $\exp(-\tau_{abs,FS})$ . This exponential cut off in flux can significantly reduce the RS emission, especially for observations at longer wavelengths, such as the radio.

## 2.5 Lepton-enriched ejecta

We include  $e^\pm$  pairs in the calculation by simply adding a certain number of pairs per ejecta proton,  $N_\pm$ , to the calculation described above. We do not calculate the creation of these pairs; we make the assumption that a certain number of pairs per proton are present in the ejecta already, either being intrinsic from the source or being created by dissipative processes during the GRB, prior to the afterglow stage.

We change the radiation calculation described above by multiplying the column density of electrons by the number of ejecta pairs,  $L \equiv 1 + 2N_\pm$  (the 1 is for the electrons already accompanying the protons in the baryonic ejecta) and by dividing the minimum electron energy by the number of pairs (i.e. the new minimum thermal Lorentz factor is  $\gamma_{ir}/L$ ). The dynamics calculation is only altered when  $N_\pm \gtrsim m_p/m_e$ . To account for the presence of a high number of pairs, we alter the dynamics calculation by reducing the number of protons in the ejecta for a fixed burst energy by  $L_{ep} \equiv 1 + 2N_\pm m_e/m_p$  (see Table 1).

The RS minimum electron thermal Lorentz factor averaged over the entire lepton population at shock crossing is

$$\gamma_{ir,+} = \frac{\varepsilon'_{er} \langle e_{p,+} \rangle L_{ep}}{m_e c^2 L}. \quad (15)$$

Since the RS is only mildly relativistic in the spreading ejecta width case, the addition of pairs to the ejecta quickly drops  $\gamma_{ir}$  into the Newtonian regime. The already low injection frequency in the reverse shock can be reduced dramatically by even modest  $L$  (see Table 1). The injection frequency of course cannot drop below the cyclotron frequency; we keep track of this in our numerical calculation.

The cooling frequency has very weak dependence on  $N_\pm$  (there is dependence on  $N_\pm$  through  $L_{ep}$ , but this only makes a difference if  $N_\pm \gtrsim 1000$ ). If  $Y \gg 1$  and  $\nu_{ir} < \nu_{cr}$ ,  $\nu_{cr} \propto L^{2(p_r-2)/(4-p_r)}$  (for  $N_\pm \ll m_p/m_e$ ). The dependence of  $\nu_{ar}$  on the pair content when  $\nu_{ir} < \nu_{ar} < \nu_{cr}$  is  $\nu_{ar} \propto L^{(4-2p_r)/(4+p_r)}$  for  $N_\pm \ll m_p/m_e$ ;  $\nu_{ar}$  is also fairly insensitive to pair content.

## 3 RESULTS

In this section, we describe the effects of IC cooling by flux generated in the RS and FS, absorption in the FS, and the effect of lepton-enriched ejecta on the RS emission, then determine if there are observable signatures of pair enriched ejecta. To ascertain the effect of each of these new additions to our calculation over the entire parameter space and a wide range of RS strengths for  $s = 0, 2$ , we randomly vary each parameter in the ranges:  $50 \leq \Gamma_0 \leq 1000$ ,  $1s \leq t_{GRB} \leq 100s$ ,  $0.1 \leq E_{52} \leq 1000$ ,  $10^{-3} \text{ cm}^{-3} \leq n_0 \leq 100$

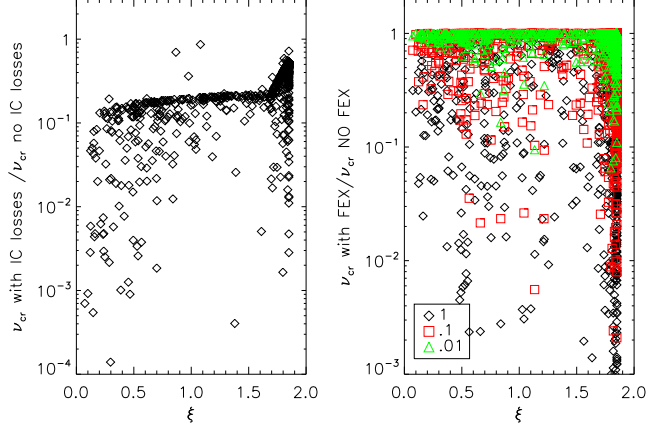


**Figure 1.** Left panel: Ratio at deceleration of numerically calculated  $\nu_{cr}$  (with IC cooling) to analytic estimate given in Table 1 (not including IC cooling) for 1000 test cases in  $s = 0$ . The inclusion of IC cooling reduces  $\nu_{cr}$  by a factor of roughly 10 over a wide range of RS strengths ( $\xi$ ). Right panel: Ratio at deceleration of numerically calculated cooling frequency without external cooling included to numerical value with external cooling included, for the also for the  $s = 0$  case. The legend gives the value of  $\varepsilon_{Bf}$  in comparison to the value of  $\varepsilon_{Br}$ , e.g. for the red squares,  $\varepsilon_{Bf} = 0.1\varepsilon_{Br}$ .

$\text{cm}^{-3}$  ( $10^{-2} \leq A_* \leq 10$  for  $s = 2$ ),  $10^{-5} \leq \varepsilon_{Br} \leq 0.1$ ,  $0.01 \leq \varepsilon_{ir} \leq 0.1$ ,  $2.01 \leq p_r \leq 2.91$ , and  $1 \leq N_\pm \leq 1000$  for 1000 test cases (synthetic GRB afterglows). All of the parameters are assumed to have uniform distributions in log space with the exception of  $p_r$ , which is assumed to have a uniform distribution. The microphysics parameter ranges were chosen to be consistent with values found from late time afterglow modeling.

### 3.1 Inverse Compton & External Cooling

In the left panel of Figure 1, the ratio of our numerical value of  $\nu_{cr,+}$  to the analytical value given in Table 1 for 1000 test cases is plotted against  $\xi$ , the dimensionless RS strength parameter, at deceleration, for  $s = 0$ .<sup>2</sup> Each RS parameter is randomly varied in the ranges described above, except for  $N_\pm$ , which is set to 0. For each of the 1000 cases, the spreading condition is evaluated at deceleration, and the numerically calculated  $\nu_{cr,+}$  is compared to the analytical value in the proper ejecta evolution case.

The numerically calculated value of  $\nu_{cr,+}$ , which includes the self consistent inverse Compton and synchrotron self absorption calculation as described in §2.2, is in general about a factor of 10 lower than the analytic value (not including IC losses) that is typically used over a wide range of RS strengths. For those cases where the numerical value

<sup>2</sup>  $\xi = (l/\Delta)^{1/2} \Gamma_0^{-4/3}$ , where  $l = (3E/(4\pi n_0 m_p c^2))^{1/3}$ ;  $\xi \ll 1$  is relativistic RS and  $\xi \lesssim 1$  is the generic, mildly relativistic RS case. For  $\xi \sim 2$ , the ejecta is in the spreading regime with a mildly to non-relativistic RS (these points are bunched very closely together in the figures, since  $\xi$  is virtually constant over the dynamics parameter space for all spreading cases), whereas the non spreading ejecta case ranges from  $\xi \ll 1$  to  $\xi \lesssim 2$ .

is even smaller, the Compton  $Y$  parameter is rather large (these cases are more abundant for the non spreading case, with relativistic RS). For  $s = 2$  (not shown in the figure), the analytical value of  $\nu_{cr,+}$  can also be less than the numerical value of  $\nu_{cr,+}$ . This is because our cooling calculation has taken into account the fraction of the synchrotron flux that has been synchrotron self-absorbed, reducing the rate of energy loss for electrons; synchrotron self-absorption contributes more to the RS cooling calculation in  $s = 2$  than  $s = 0$ .

External flux influences the RS cooling calculation by decreasing  $\nu_{cr}$ . If the FS radiation was produced with  $\varepsilon_{Bf} \sim \varepsilon_{Br}$ , the external flux can lower  $\nu_{cr}$  via IC scattering by up to a few orders of magnitude for both  $s = 0, 2$  cases. The effect of external flux IC cooling on the RS synchrotron flux near deceleration in most cases is relatively small; the effect is greatest in the x-ray band, where  $\nu_{obs} > (\nu_{ar}, \nu_{ir}, \nu_{cr})$ , and flux here can be decreased by a factor of a few (IC flux is also an important contributing factor to the total light curve in the x-ray, and is not considered here). The more important effect of the external flux is to decrease the cooling frequency below the R band on a shorter time scale after deceleration, causing the light curve to fall off very steeply, as  $\sim 1/t^3$ , soon after deceleration. Overall, the effect of external flux on electron cooling makes RS synchrotron emission a little fainter at the peak of the light curve and fall off faster after deceleration, making the RS synchrotron emission more difficult to detect.

In the right panel of Figure 1, we show the effect of adding external cooling to our calculation. We plot the ratio of the numerically calculated  $\nu_{cr,+}$  without external cooling to  $\nu_{cr,+}$  including external cooling from the FS. We let  $p_f = p_r$ ,  $\varepsilon_{if} = \varepsilon_{ir}$ , and try three cases of  $\varepsilon_{Bf} = (1, 0.1, 0.01)\varepsilon_{Br}$ . With external cooling included,  $\nu_{cr}$  in either the spreading or non spreading case can be reduced by up to 3-4 orders of magnitude! This is true over a wide range of RS strengths, and also for  $s = 2$ . The effect is strongest when  $\varepsilon_{Bf} = \varepsilon_{Br}$  and weakest when  $\varepsilon_{Bf} = 0.01\varepsilon_{Br}$ .

### 3.2 Effect of Absorption in FS

Absorption of RS synchrotron photons in the FS is most important in the radio, as the FS self absorption frequency lies in this band. In a large part of the parameter space, the low frequency ( $\sim 4$  GHz) RS flux can be completely absorbed; in another run of 1000 different RS cases (varying the parameters as described above, and setting FS  $\varepsilon_{if}$ ,  $\varepsilon_{Bf}$ , and  $p_f$  equal to RS values), we find that in approximately 15% of 1000 test cases, the RS radio (8.5 GHz) flux is completely absorbed by the FS material. In approximately 40% of the test cases,  $\tau_{abs,FS} > 1$  (including those cases where the RS radio flux is completely absorbed), meaning that the RS radio flux was decreased by at least a factor of 3. If we set  $\varepsilon_{Bf} = \varepsilon_{Br}/100$ , we find that 12% of 1000 test cases are completely absorbed in the FS, and in 23% of the cases,  $\tau_{abs,FS} > 1$ . Absorption in the FS may turn out to be a contributing factor to the difficulty in observing RS flux in the radio.

### 3.3 RS Emission with Pair-Enriched Ejecta

Adding a certain number of pairs per proton to the ejecta adds another parameter to the RS flux calculation, bringing the total number of parameters in the RS to four, viz.  $\varepsilon_{ir}$ ,  $\varepsilon_{Br}$ ,  $p_r$ , and  $N_{\pm}$ <sup>3</sup>. We need four independent measurements of the RS emission to constrain these four parameters. Flux in the optical & X-ray at early times, spectral index and radio flux at  $\sim 0.1$  day are four quantities that can be observed with the current generation of instruments.

For  $\nu_{obs} > (\nu_{ir}, \nu_{cr}, \nu_{ar})$  (x-ray) with  $Y \ll 1$  or  $\nu_{ir} < \nu_{ar} < \nu_{obs} < \nu_{cr}$  (optical) for any  $Y$ , the observed flux at deceleration has a dependence on  $N_{\pm}$  of

$$f_{\nu} \propto \frac{L^{(2-p_r)}}{L_{ep}^{5(2-p_r)/4}}. \quad (16)$$

For  $p_r \sim 2$ , this flux depends very weakly on the number of pairs in the ejecta. For  $p_r > 2$ , the x-ray and optical flux are decreased from the  $N_{\pm} = 0$  case as  $N_{\pm}$  is increased (for  $N_{\pm} \ll m_p/m_e$ ), but the shape of the light curve does not change (i.e. no breaks are introduced by reducing the injection frequency below the low value at which it already sits in the absence pairs in the ejecta).

In the radio, the observer flux for  $\nu_{obs} < \nu_{ir} < \nu_{ar} < \nu_{cr}$  is proportional to  $L^{-1}L_{ep}$ . The flux in the radio is the most greatly affected by the addition of pairs to the calculation, so the best possible place to look for a signature of pair-enriched ejecta is in the radio wavelengths. In Figure 2, we plot an example of RS and FS radio light curves (8.5 GHz) without pairs (for burst parameters see figure caption) compared to three cases: (1) adding 100 pairs/p to the ejecta, (2) decreasing  $\varepsilon_{Br}$  by a factor of 10, and (3) decreasing  $\varepsilon_{ir}$  by a factor of 10. All three of these actions produce very similar RS radio light curves; the situation is highly degenerate, and it would be difficult to distinguish the effect of pairs in the ejecta on the emission from a variation in the microphysics parameters in the RS.

1000 RS test cases (parameters varied over ranges described above with no external cooling or absorption in the FS) show that the peak frequency of  $f_{\nu}$ , at  $\max\{\nu_{ar}, \min\{\nu_{ir}, \nu_{cr}\}\}$ , at deceleration also has very little, if any, dependence on the number of pairs in the ejecta for  $s = 0, 2$ . This is also true if external cooling is included in the calculation. This is in contradiction to the conclusion that Li et al. (2003) came to; this is because, over a large portion of the parameter space, the peak of the spectrum in both the baryonic and pair-enriched cases is at  $\nu_{ar}$ , and  $\nu_{ar}$  has little dependence on the number of pairs in the ejecta.

Thus, we conclude there is no single wavelength light curve signature that depends only on the pair content of the ejecta, and not on the microphysics parameters in the RS as well.

<sup>3</sup> FS microphysics parameters and the energy in the explosion, external density, and initial jet opening angle can be determined, as has been done in the past, by late-time FS light curve fitting when the RS makes a small contribution to the total flux.

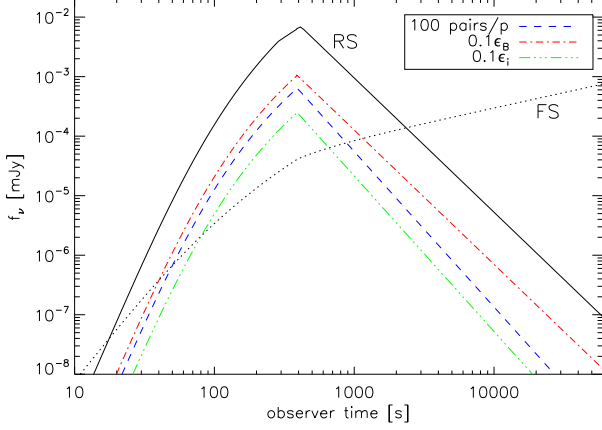


**Figure 2.** Radio (8.5 GHz) light curve for  $s = 0$  with the input parameters  $E_{52} = 3$ ,  $\Gamma_0 = 160$ ,  $t_{GRB} = 4$  s,  $n_0 = 1.6 \times 10^{-3} \text{ cm}^{-3}$ ,  $\epsilon_{Br} = \epsilon_{Bf} = 4 \times 10^{-5}$ ,  $\epsilon_{ir} = \epsilon_{if} = 0.09$ ,  $p_r = p_f = 2.5$ ,  $N_{\pm} = 0$ , and  $z = 1$ . External cooling and absorption in the FS are not included in this calculation. The solid line represents the RS light curve with the above parameters and the FS emission is shown by the dotted line. The three colored lines alter the parameters in the calculation as detailed in the legend.

### 3.4 Using Optical and Radio Observations to Determine Pair Content

The best way to discriminate between baryonic and pair-enriched ejecta is by comparing flux at low frequencies (radio band) and the optical band. NP04 suggested a particular combination of the ratio of observed RS optical and radio fluxes at the peak of each respective light curve and the ratio of the observer times at which these peaks occur as a way of determining if the radiation is from the reverse shock. We use a similar combination to decide whether the ejecta is pair enriched.

The parameter we use to determine the pair-enrichment ( $\chi$ ) is slightly different than that in NP04 (note the difference in exponents on the ratio of observer times),

$$\chi \equiv \left(\frac{F_*}{F_0}\right) \left(\frac{t_*}{t_0}\right)^k = \left(\frac{\nu_{opt}}{\nu_{radio}}\right)^{\frac{(p_r-1)}{2}} \sim 1000 \quad (17)$$

where

$$k \equiv \begin{cases} \frac{5(p_r-1)}{6} + \frac{9}{8} & s = 0 \\ (p_r - 1) + \frac{5}{6} & s = 2 \end{cases} \quad (18)$$

and are determined analytically using decay indices after deceleration of  $\nu_{ir} \propto t^{-5/3}$  and  $F_{pr} \propto t^{-9/8}$  for  $s = 0$  and  $\nu_{ir} \propto t^{-2}$  and  $F_{pr} \propto t^{-5/4}$  for  $s = 2$  (assuming spreading ejecta evolution for both cases). As in NP04,  $t_0$  is the observer time peak of the optical RS emission,  $t_*$  is the observer time peak of the radio RS emission (the peak is produced when  $\nu_{ar}$  falls below the radio), and  $F_0$  &  $F_*$  are the observed fluxes at these two points. The shell width at deceleration in both shell evolution cases is  $\sim R_+/\Gamma_+^2$  which is  $\ll R^4$ , so time delay between photons arising from the front

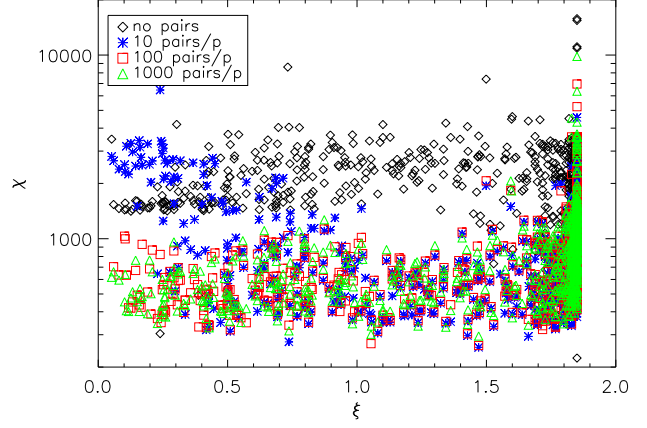


**Figure 3.**  $\chi$  for  $p_r = 2.5$  and  $s = 0$  for 1000 test RS numerical light curves, excluding absorption of RS photons in the FS and external cooling. We randomly vary all RS parameters but  $p_r$  and  $N_{\pm}$ ; other values of  $p_r$  give qualitatively similar results when adding leptons to baryonic ejecta, however  $\chi$  for the reference purely baryonic case is higher for higher  $p_r$  and vice versa.  $s = 2$  has qualitatively similar results which are discussed in §3.4. The scatter in each case is caused for the most part by the variation in dynamics parameters. There are some points with very low  $\chi$  cut off of the bottom of the plot; these are caused when  $\nu_{ar} > \nu_{cr}$ , and  $\nu_{ar}$  tracks  $\nu_{cr}$  in time (which evolves more quickly, leading to smaller  $t_*$ ).

and back ends of the shell has small effect on the observed flux.

We plot  $\chi$  in Figure 3 versus the dimensionless RS strength parameter,  $\xi$ , in a run of 1000 RS cases as described in § 3, except that  $p_r$  is held fixed at 2.5 and  $N_{\pm}$  is held constant for each case. External cooling and absorption in the FS were turned off. For  $N_{\pm} = 0$ , the value for  $\chi$  can be larger or smaller by a factor of a few from 1000 for a constant value of  $p_r \sim 2.5$ , and is fairly constant over a large range of reverse shock strengths. There are a few points which are cut off the bottom of the plot with abnormally low  $\chi$ —these points are caused by  $\nu_{cr}$  falling below  $\nu_{ar}$ . When this happens,  $\nu_{ar}$  tracks  $\nu_{cr}$  (since there are no electrons radiating above  $\nu_{cr}$  after the RS reaches the rear of the shell), which evolves more quickly than  $\nu_{ar}$  does when  $\nu_{ar} < \nu_{cr}$ , making  $t_*$  and  $F_*$  smaller. This scenario is easily detected by checking the decay of the radio light curve after the peak; if the decay is steep, like  $\sim 1/t^3$ , the abnormally low value of  $\chi$  is due to  $\nu_{cr}$  falling below the radio band with  $\nu_{ar}$ .

When pairs are added to the ejecta, we find that for  $N_{\pm} \gtrsim 100$ , the value of  $\chi$  has dropped by a factor of about 5 for the parameter space with  $\xi \lesssim 1.6$  (ultra-relativistic to mildly relativistic RS). For  $N_{\pm} = 10$ , the value for  $\chi$  ranges from  $\sim 3000$  when the RS is relativistic ( $\xi \ll 1$ ) to  $\sim 200$  when the RS is mildly to non relativistic, making it difficult to distinguish between baryonic and pair enriched ejecta. Compared with the range of  $\chi$  for baryonic ejecta (greater or less than 2000 by a factor of about 2), the drop in  $\chi$  by a factor of 5 for  $N_{\pm} \gtrsim 100$  could possibly be used as a tool to distinguish the pair content of the ejecta. So, if observations are available for a burst at the peak of the R band and radio RS emission, and  $p_r$  is able to be determined from

<sup>4</sup> This is true in the non spreading case because of causality—the distance traveled by the shock front in the shell comoving frame is of order  $R_+/\Gamma_+$ , which is  $R_+/\Gamma_+^2$  in the lab frame



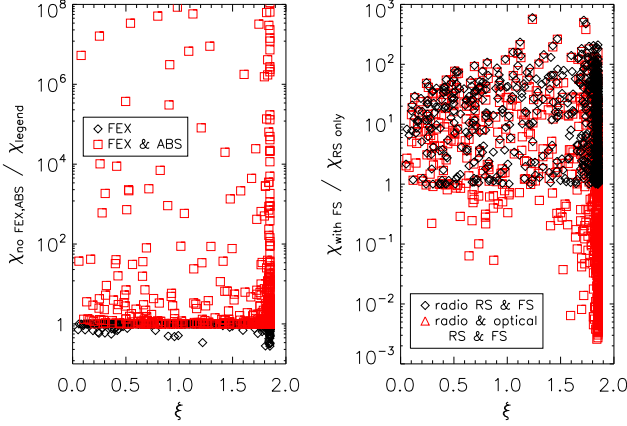


**Figure 4.** Left panel: Ratio of  $\chi$  (no pairs) without external flux or absorption in the FS to  $\chi$  with external flux and absorption in the FS plotted against the value of  $\xi$  at deceleration. Note that the ratio including absorption can go to arbitrarily high numbers, since radio flux can be completely absorbed ( $\chi = 0$  with absorption in FS in these cases); some of these points have been cut off the plot. Right panel: Ratio of  $\chi$  calculated including contributions of FS in just the radio and in both the radio and optical band to  $\chi$  calculated without FS contribution, plotted against  $\xi$  at deceleration.

spectra, we can calculate  $\chi$  and determine if  $N_{\pm} \gtrsim 100$  (it is not possible to determine the exact number of pairs per proton, but only if  $N_{\pm} \gtrsim 100$ ). It will be extremely difficult to tell if the ejecta has a pair content of  $N_{\pm} \lesssim 100$ .

In Figure 4, in the left panel,  $\chi$  is shown including the effect of adding external cooling and FS absorption to the purely baryonic ejecta case. We repeat the calculation of 1000 test cases with  $p_r = 2.5$  and  $N_{\pm} = 0$ , and we set  $p_f = p_r$ , and vary  $\varepsilon_{if}$  and  $\varepsilon_{Bf}$  in the same ranges as the corresponding RS parameters. The inclusion of external cooling in the calculation does not affect  $\chi$  much. The value of  $\chi$  is increased at most by a factor of a few from the calculation without external cooling included, and still lies within the scatter for the baryonic case shown in Figure 3.

Including absorption in the FS, however, will invalidate Equation 17, since we assumed in deriving it that the RS radio flux at the light curve peak is equal to the flux at the peak of the RS spectrum at  $t_*$ . This decrease in  $F_*$  by a large factor also decreases  $\chi$  by the the same factor ( $\chi$  in this case could be  $\lesssim 1$ ). In §3.2, we found that absorption in the FS can be a large effect for much of the parameter space at 8.5 GHz. Absorption in the FS for observer frequencies less than  $\sim 10$  GHz may indeed make it more difficult to accurately determine the pair content of the ejecta. However, at higher frequencies,  $\sim 100$  GHz, FS absorption is less important and one can calculate  $\chi$  at these frequencies to determine  $N_{\pm}$  (note that  $\chi$  will be a factor of a few smaller at higher radio frequencies for the purely baryonic case).

To determine if  $\chi$  for  $s = 2$  has similar properties to the  $s = 0$  case, we carry out a numerical simulation of 1000 RS test cases for  $s = 2$  identical to that done for  $s = 0$  (without external cooling or absorption), finding qualitatively similar results as the  $s = 0$  case. With  $N_{\pm} \lesssim 100$ , the pair content is difficult to determine, but for  $N_{\pm} \gtrsim 100$ , the value of  $\chi$  is

about a factor of 5 lower than in the baryonic case. In the purely baryonic case,  $\chi \sim 3000$  for  $s = 2$  and this value ranges between a factor of 3 higher and lower. The spread of  $\chi$  values here is larger because the range of  $n_0 = AR^{-s}$  for  $s = 2$  is larger than the range of  $n_0$  chosen for the  $s = 0$  case.

Up to this point, we have not considered the contaminating effect of the FS emission to the optical or radio RS emission at the RS light curve peaks. It may be most difficult to distinguish RS from FS flux in observed radio light curves, so we calculate the value of  $\chi$  with the FS radio flux included. In the right panel of Figure 4, we've plotted the ratio of  $\chi$  calculated (for  $s = 0$ ) with the FS radio flux contribution to  $\chi$  without FS flux at the time which the RS radio light curve peaks. Again, for 1000 test cases, we set  $p_f = p_r$ , set  $N_{\pm} = 0$ , and vary  $\varepsilon_{if}$  and  $\varepsilon_{Bf}$  in the same ranges as the corresponding RS parameters. We find that the value of  $\chi$  can increase by a factor of up to 100 from the RS only case, outside of the scatter in  $\chi$ . In 60% of the 1000 test cases, the FS radio contribution was greater than the RS radio contribution at the RS radio peak. For  $s = 2$ , this occurs in 83% of the 1000 test cases. One needs to separate the contribution of the RS and FS to the radio flux using late time data in order to use this tool reliably to determine the ejecta pair content.

If the RS radio peak was observed, but the light curve has significant FS contribution, it may be possible to separate the contribution of FS from the RS radio flux by continued monitoring of the radio band for a period of a week or so, when the FS radio LC peaks. This information can be used to determine the contribution of the FS to the radio flux at the time of the RS peak, and  $\chi$  due to the RS alone. If the radio flux is dominated by the FS contribution during the RS peak and the RS peak is not observed, then this tool cannot be used to determine ejecta pair content.

We also find that the optical RS peak may be as difficult to observe as the radio peak due to FS contamination, in agreement with the conclusion drawn in NP04. In the right panel of Figure 4, we also show the ratio of  $\chi$  with FS contribution (both radio and optical) to  $\chi$  with only RS flux. The inclusion of FS optical flux at deceleration increases the scatter in  $\chi$  even more;  $\chi$  with FS flux ranges from being 100 times smaller to 100 times larger than  $\chi$  with RS flux only. For the  $s = 0$  case, the FS optical flux at deceleration is brighter than the RS optical flux 70% of 1000 test cases; in the  $s = 2$  case, this occurred in only 30% of 1000 test cases. This is another difficulty in calculating  $\chi$  for observed light curves. However, as in the radio, if an RS optical peak is observed, the FS contribution may be able to be removed if the optical light curve is followed for long enough after deceleration to determine the FS contribution to the total observed flux. We note that the fact that the FS optical emission is larger than the RS optical emission at deceleration in  $\sim 70\%$  of test cases for  $s = 0$  may explain the lack of optical flashes and rapidly declining light curves at detected early times.

Scintillation in the radio may also be a problem for observing the RS radio peak due to the high level of variability that this process introduces into the observed radio light curve, as was observed in GRB 970508 (Frail et al. 1997; Taylor et al. 1997). The fluctuations are more pronounced at early times, when the RS radio light curve is

expected to peak, because the source size is smaller. One can reduce fluctuations from scintillation by observing at frequencies higher than 8.5 GHz. Observations made at frequencies near 50 GHz and even in the millimeter range (250 GHz) may be more suitable for determining  $\chi$  and  $N_{\pm}$  because of the insensitivity to scintillation at these frequencies. The effect of absorption in the FS is also smaller for these higher energy radio photons ( $\tau_{abs,FS} > 1$  for a much smaller parameter space), and the RS light curve peaks at earlier times at these frequencies when the FS light curve may not be as bright. With current technology, radio observations on the timescales necessary for calculating  $\chi$  of few minutes/hours to days after the burst are feasible at around 8.5 GHz. At higher frequencies like the sub-millimeter, recent observations are typically being done  $\sim 0.1$  to 1 day post-burst (Smith et al. 2005); the timescale for the sub-millimeter light curve peak is from a few minutes to a few hours after the burst (up to about 0.1 day).

Other things that may limit the usefulness of  $\chi$  as a tool for estimating  $N_{\pm}$  include sparseness of sampling of the radio light curve near the RS and FS peaks and breaks in the electron energy distribution between the optical and radio. The sparseness of radio data points near the RS and FS light curve peaks may introduce an error into the determination of  $\chi$  of a factor of a few. Panaitescu & Kumar (2002) have found evidence in late-time afterglow modeling of a break in the electron energy distribution between the radio and the optical; one must be careful to choose the correct value of  $p_r$  (value of  $p_r$  between  $\nu_{ir}$  and the optical band) for the calculation of  $\chi$ .

In summary, it is possible to use optical and radio flux and observer times at the respective peaks of the light curves to determine pair content if the number of pairs/proton is  $\gtrsim 100$ . There are many factors, however, that one must take into account when using this tool. The contributions to the optical and radio flux from the RS and FS must be separated, which may be difficult and requires good time coverage from  $\sim 1$  minute to hours in the optical and  $\sim 1$  hour to days in the radio. In the radio band, below 10 GHz, absorption in the FS and interstellar scintillation pose problems, and in order to avoid these issues, one should use observations at a higher frequency than  $\sim 100$  GHz.

### 3.5 Constraining Parameters with Available Observations and Upper Limits

In Figure 5, we plot the comparison of our numerically calculated R band flux at deceleration with the full analytical expression given in the last row of Table 1 ( $p = 2.5$  and  $z = 1$ ) and in Appendix A (full expression). The numerical calculation does not include external cooling or absorption in the FS (the latter is unimportant for the R band, but the former could decrease the flux by a factor of  $\sim 2$ ), and all parameters are varied, including  $N_{\pm}$ . The analytical expressions assume  $(\nu_{ir}, \nu_{ar}) < \nu_{obs} < \nu_{cr}$  and include pairs. For each case of  $s = 0$  or  $s = 2$ , we ran 1000 test cases, and separated these 1000 cases into two sets determined by their ejecta width at deceleration. The blue line shown on each plot shows a linear relationship for a guide, and the orange line shows the relationship if the numerical flux were 10 times the analytically calculated flux.

In all four cases, the scatter around the linear relation-

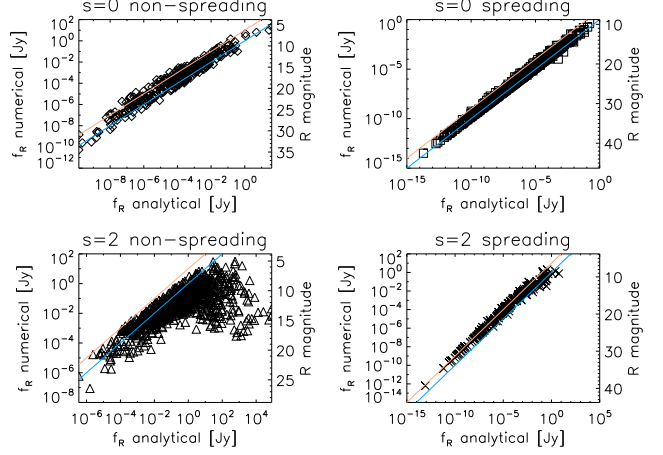


**Figure 5.** Comparison of 1000 test cases of numerically calculated R-band flux at deceleration with analytical expression for each case of  $s = 0, 2$  spreading/non-spreading. All parameters, including  $N_{\pm}$ , are varied. The full analytical expressions assume  $(\nu_{ir}, \nu_{ar}) < \nu_{obs} < \nu_{cr}$  and are given in the last row of Table 1 for the case of  $p = 2.5$ ,  $z = 1$  and in Appendix A for the general case. A linear relationship (blue line) and  $f_R$  analytical = 10 times  $f_R$  numerical (orange line) are shown on each panel for a guide.

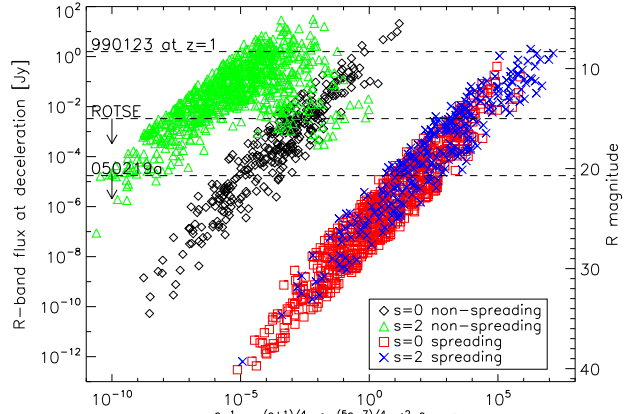


**Figure 6.** Observer frame RS flux in the R-band at deceleration assuming  $z = 1$  and including pairs (no external cooling or absorption in the FS) plotted against the parameter dependences in the expression for flux in the R band at deceleration (without constants). All parameters are varied. The variable  $D$  in the expression on the x-axis contains all of the dynamics parameters and is different for each of the four cases shown:  $D = n_0^{p_r/4} \Gamma_0^{p_r-2} E_{52}^{5/4} t_{dur}^{-3/4}$  for  $s = 0$  non-spreading,  $A_*^{p_r/2} \Gamma_0^{p_r-2} E_{52}^{(5-p_r)/4} t_{dur}^{-(3+p_r)/4}$  for  $s = 2$  non-spreading,  $n_0^{(p_r+1)/4} \Gamma_0^{p_r} E_{52}$  for  $s = 0$  spreading, and  $A_*^{3(1+p_r)/4} \Gamma_0^{1+2p_r} E_{52}^{(1-p_r)/2}$  for  $s = 2$  spreading. The three dashed lines denote the observed R band flux at deceleration for GRB 990123 shifted to  $z = 1$ , observed upper limits reported in Kehoe et al. (2001) from the ROTSE telescope, and the V-band upper limit reported by Swift UVOT for GRB 050219a (Schady et al. 2005), shown for comparison to expected theoretical R band flux from the RS. Note that 990123 was an exceptional burst—a very small fraction of the parameter space produces optical flashes this bright.

ship is due to the estimations made for  $\Gamma_{ej}$  and more importantly  $\gamma_{ir}$  in the analytical expression.  $\gamma_{ir}$  is more difficult to estimate in the non spreading case, since the range of RS strengths ranges from ultra-relativistic to Newtonian. Since we use a mildly relativistic RS estimate for the analytical expression, the analytical expression underestimates the ultra-relativistic RS flux and overestimates the Newtonian RS flux. Likewise, in the spreading case, we made an estimate of  $\gamma_{ir}$  being mildly relativistic; all spreading cases are mildly relativistic to Newtonian, so the scatter around a linear relationship is much smaller than for non spreading ejecta. There is still a small bit of scatter due to the value of  $\gamma_{ir}$  that we chose (see Table 1), and the analytical value is typically within a factor of a few to 10.

The analytical expression given in Table 1 is a good estimation of the R band flux at deceleration for both spreading cases. It is less useful for the non spreading cases; in the  $s = 2$  non-spreading case, the ordering of break frequencies assumed in the analytical expression is often not applicable, and the linear relationship does not hold over the entire parameter space explored—this occurs in the top right hand corner of the plot for this case. The cooling frequency is typically lower in  $s = 2$  compared to  $s = 0$ , and drops below the other two break frequencies frequently in this calculation.

In Figure 6, we have done the same calculation as described above for Figure 5, only here we have plotted the numerical observer frame R band flux against only the parameter dependences from the analytical expression for R band flux. For example, for  $s = 0$ ,  $\Delta = R_+/(2\Gamma_0^2)$ , we have plotted numerically calculated RS flux  $f_\nu$  against the analytical combination of parameters  $\varepsilon_{ir}^{p_r-1} \varepsilon_{Br}^{(p_r+1)/4} L^{2-p_r} n_0^{(p_r+1)/4} \Gamma_0^{p_r} E_{52}$ . The scatter (width) of the spreading regions on this plot are mainly due to the variation of  $p_r$ , while the scatter of the non spreading regions is due to  $p_r$  and the dynamics parameters. The  $s = 2$  non spreading case is again not quite linear, for reasons discussed above for Figure 5.

This plot can be used as a tool to constrain the burst parameters using observed R-band flux or upper limits at or near deceleration using the more accurate results of the numerical calculation. Also, this plot can be used to view the ranges of expected R-band flux at deceleration if the early afterglow is caused by the RS with baryonic or pair enriched ejecta. Lines are drawn onto the plot to compare to the early afterglow detection of GRB 990123 at the peak (scaled from  $z = 1.61$  to  $z = 1$ ) and upper limits from ROTSE and *Swift*.

We find that optical flash emission from GRB 990123 falls at the very bright end of the distribution of RS R band flux at deceleration for all 4 cases shown in Figure 6. There are a great many synthetic bursts in our calculation, especially in the case of  $s = 0$ , spreading ejecta, with intrinsically low R band RS flux levels for burst parameters consistent with those found from afterglow modeling. This may indeed be the reason that the growing number of GRBs with rapid follow up do not show a bright optical flash.

As an example of how to use Figure 6 to constrain burst parameters with optical data or upper limits near deceleration, we look at the case of GRB 050219a. GRB050219a was a 23.6 s long *Swift*-detected burst of with a fluence of  $(5.2 \pm 0.4) \times 10^{-6}$  erg cm $^{-2}$  and was detected in the x-ray by XRT (Romano et al. 2005). An optical upper limit from *Swift* of  $V = 20.7$  was found 96 s after the burst

(Schady et al. 2005). We find that the upper limit for this burst falls near the bottom of the distribution of the non-spreading cases (although the distribution can be extended to lower values of  $f_{\nu,R}$  using even lower limits for the ranges on  $n_0/A_*$  and  $\varepsilon_{Br}$ ) but is in the middle of the distribution for the two spreading cases. It seems that RS flux fainter than this upper limit is fairly typical in the case of spreading ejecta.

Using Figure 6, we can make constraints on the burst parameters of 050219a (assuming that the upper limit of  $V = 20.7$  applies at deceleration for this burst and there was no extinction). In the  $s = 2$  cases, we can make fairly severe constraints on  $\varepsilon_{Br}$  and  $A_*$ . For example, using the plot for the  $s = 2$  non spreading case, if we assume  $z = 1$  (although see Berger et al. 2005 for the redshift distribution for *Swift* GRBs so far) and  $p_r \sim 2.2$  we find (see Table 1)

$$\varepsilon_{ir}^{1.2} \varepsilon_{Br}^{0.8} L_{ep} L^{-0.2} A_*^{1.1} \Gamma_0^{0.2} E_{52}^{1.8} t_{dur}^{-1.3} \lesssim 1.2 \times 10^{-8}. \quad (19)$$

Using the observed burst duration and using the assumption  $z = 1$ ,  $t_{dur} = 11.8$  s, and estimating  $E_{52}$  from the fluence, we set  $E_{52} \sim 2$ . We set  $\varepsilon_{ir} = 0.1$ , a typical value, as indicated from afterglow modeling (Panaiteescu & Kumar 2002). Inserting these values and setting  $\Gamma_0 = 100\Gamma_{0,2}$ , we have

$$\varepsilon_{Br}^{0.8} L^{-0.2} A_*^{1.1} \Gamma_{0,2}^{0.2} \lesssim 5.3 \times 10^{-7}. \quad (20)$$

Since the dependence of this relation on the number of pairs and  $\Gamma_{0,2}$  is small, we can say that within a factor of a few,  $A_*^{1.1} \varepsilon_{Br}^{0.8} \lesssim 5.3 \times 10^{-7}$ , implying very small values for  $A_*$  and/or  $\varepsilon_{Br}$ .

If we set  $\varepsilon_{Br} \sim 10^{-5}$ , on the lower end of the distribution of values found from afterglow modeling (Panaiteescu & Kumar 2002),  $A_* \lesssim 10^{-2}$ . Also, if we choose to make  $\varepsilon_{ir}$  smaller for this burst than the typical value we have chosen, say  $\varepsilon_{ir} \sim 0.01$ , then if  $A_* \sim 1$ ,  $\varepsilon_{Br} \lesssim 10^{-7}$ , still a rather low value.

If we try the  $s = 2$  spreading case, we find similarly severe requirements for  $A_*$  and  $\varepsilon_{Br}$ . The expression for the spreading case, however, is much more sensitive to  $\Gamma_{0,2}$ , so the limits on  $A_*$  and  $\varepsilon_{Br}$  are not as robust as in the non spreading case above. For  $A_* \sim 1$  and  $\Gamma_{0,2} \sim 1$ ,  $\varepsilon_{Br} \lesssim 10^{-9}$ . If we require  $\varepsilon_{Br} \sim 10^{-5}$ , then  $A_* \sim 0.1$ . In summary, for the  $s = 2$  density profile to apply, with either spreading or non spreading ejecta, the upper limit at 96 s requires low values of  $A_*$  or  $\varepsilon_{Br}$  near deceleration. For the  $s = 0$  cases, using the typical values above ( $\varepsilon_{ir} \sim 0.1$ ), we find the optical upper limit at 96 s to be less constraining on  $n_0$  and  $\varepsilon_{Br}$ .

## 4 DISCUSSION

In this paper, we have calculated RS emission from purely baryonic and pair-enriched ejecta. We take into account the mildly relativistic nature of the RS (we allow for the full range of RS speeds, from Newtonian to ultra-relativistic), and self consistently calculate synchrotron self absorption and inverse Compton cooling in the ejecta. Additionally, we have allowed for the ejecta to be cooled by FS synchrotron flux incident on the ejecta and for the low-energy RS photons to be absorbed in the FS material as they move outward from the source.

We find that the flux in the R band at deceleration depends very weakly on the ejecta pair content. The RS radio

emission is affected by ejecta pairs the most, however the shape of the radio light curve is not affected. The effect of pairs on any single wavelength light curve (a reduction in the flux with increasing number of pairs per proton) can be replicated by varying the shock microphysics parameters in the RS; it is a degenerate problem. It is impossible to determine the pair content of the ejecta from a single wavelength light curve.

It may be possible to determine if  $N_{\pm} \gtrsim 100$  by using observations of the RS optical and radio light curve peaks. By calculating  $\chi$  (see Equation 17) using observations, one may be able to determine if  $N_{\pm} \gtrsim 100$ ; one cannot determine the precise number of pairs per proton with  $\chi$ , but whether there are a significant number of pairs present in the ejecta. The value of  $\chi$  for purely baryonic ejecta is fairly constant (for a given value of  $p_r$ ) over a wide range of RS strengths; effects that may increase the spread in  $\chi$  (reducing the effectiveness of  $\chi$  as a tool for determining ejecta pair content) include absorption of radio RS photons in the FS, contribution of the FS emission to the RS flux at the light curve peaks, and scintillation in the radio light curve. External (FS synchrotron) flux incident on the ejecta has little effect on the value of  $\chi$ . By using radio observations at higher frequencies, e.g. at 50 GHz or 250 GHz (mm), effects of scintillation and FS contribution to radio emission can be reduced, and  $\chi$ , and therefore the pair content of the ejecta, can be more accurately determined.

Li et al. (2003) have also looked at the emission from pair enriched ejecta; we agree that it is possible for a large number of pairs to be present in the ejecta and that the resulting R band flux is largely insensitive to the number of pairs in the ejecta, however we come to different conclusions regarding the resulting ejecta emission. Li et al. (2003) predict a strong flash in the IR band; we find that the peak frequency of the RS is largely unaffected by the pair content of the ejecta. Indeed, the injection frequency is reduced greatly by even a modest number of pairs, however we find that in the most frequent arrangement of frequencies, the peak of  $f_\nu$  is at  $\nu_{ar}$ , which is not affected by pairs much at all. Most of the difference between our calculations result from the treatment of RS strength; we have taken into account the mildly relativistic nature of the reverse shock, where Li et al. (2003) have approximated the RS as being highly relativistic. Another contributing factor to the difference in our results is the more careful and self consistent calculation of synchrotron cooling and self absorption frequencies that we have done here.

In conclusion, RS emission from pair-enriched ejecta looks very similar to that from purely baryonic ejecta. The most promising tool to determine if GRB ejecta is pair-enriched, by the measurement of the parameter  $\chi$  defined in Equation 17, depends greatly on well sampled observations near the peak of the light curves in the optical and the radio; if the optical flash is seen quickly after the burst with *Swift* or other ground based telescopes, radio follow up in frequency bands between 50 GHz and 250 GHz (mm) from 15 minutes to  $\sim 1$  day should provide some information about the pair enrichment of the ejecta.

This research was supported in part by grants from NSF (AST-0406878) and NASA-Swift (NNG05G185) (PK) and the US-Israel BSF (TP).

## REFERENCES

- Akerlof, C., et al. 1999, *Nature*, 398, 400  
 Berger, E., et al. 2005, *ArXiv Astrophysics e-prints*, arXiv:astro-ph/0505107  
 Blake, C. H., et al. 2005, *Nature* 435, 181  
 Fan, Y., Dai, Z., Huang, Y., & Lu, T. 2002, *Chinese Journal of Astronomy and Astrophysics*, 2, 449  
 Frail, D. A., Kulkarni, S. R., Nicastro, S. R., Feroci, M., & Taylor, G. B. 1997, *Nature*, 389, 261  
 Kehoe, R., et al. 2001, *ApJ*, 554, L159  
 Kumar, P., & Panaitescu, A. 2000, *ApJ*, 541, L51  
 Kumar, P., & Panaitescu, A. 2003, *MNRAS*, 346, 905  
 Li, Z., Dai, Z. G., Lu, T., & Song, L. M. 2003, *ApJ*, 599, 380  
 McMahon, E., Kumar, P., & Panaitescu, A. 2004, *MNRAS*, 354, 915  
 Meszaros, P., & Rees, M. J. 1994, *MNRAS*, 269, L41  
 Nakar, E., & Piran, T. 2004, *MNRAS*, 353, 647  
 Panaitescu, A., & Kumar, P. 2002, *ApJ*, 571, 779  
 Panaitescu, A., & Kumar, P. 2004, *MNRAS*, 353, 511  
 Romano, P., et al. 2005, *GCN* 3036  
 Rykoff, E., Schaefer, B., & Quimby, R. 2005, *GCN* 3116  
 Sari, R., & Piran, T. 1999, *ApJ*, 520, 641  
 Schady, P., et al. 2005, *GCN* 3039  
 Smith, I. A., et al. 2005, *A&A*, 439, 987  
 Taylor, G. B., Frail, D. A., Beasley, A. J., & Kulkarni, S. R. 1997, *Nature*, 389, 263  
 Vestrand, W. T., et al. 2005, *Nature*, 435, 178  
 Wijers, R. A. M. J., & Galama, T. J. 1999, *ApJ*, 523, 177  
 Zhang, B., Kobayashi, S., & Mészáros, P. 2003, *ApJ*, 595, 950  
 Zhang, B., & Kobayashi, S. 2005, *ApJ*, 628, 315

## APPENDIX A: R BAND FLUX AT DECELERATION

Here we write the full analytic expressions for the R band flux at deceleration (in cgs units) for each of the four cases in Figure 5.

$$f_{\nu,R} = \frac{\sigma_T \varepsilon_{ir}^{p_r-1} \varepsilon_{Br}^{\frac{(p_r+1)}{4}} L_{ep}^{\frac{(5p_r-7)}{4}} L^{2-p_r} (1+z)^{\frac{(1-p_r)}{2}}}{H_0^2 (\sqrt{1+z}-1)^2} \times$$

$$\left\{ \begin{array}{ll} \frac{0.018(5.2 \times 10^{16})^{\frac{(1-p_r)}{2}} m_p^{\frac{(5p_r-8)}{4}} n_0^{\frac{p_r}{4}} \Gamma_0^{p_r-2} E_{52}^{\frac{5}{4}}}{m_e^{\frac{(3p_r-5)}{2}} q^{\frac{(3-p_r)}{2}} \pi^{\frac{(6+p_r)}{4}} c^{\frac{9}{4}} t^{\frac{3}{4}} \frac{d_{ur}}{c}} & s = 0 \text{ } ct_{dur} \\ \frac{0.086(5.8 \times 10^{14})^{\frac{(1-p_r)}{2}} A_*^{\frac{p_r}{2}} \Gamma_0^{p_r-2} E_{52}^{\frac{(5-p_r)}{4}} m_p^{\frac{(3p_r-4)}{2}}}{m_e^{\frac{(3p_r-5)}{2}} q^{\frac{(3-p_r)}{2}} \pi^{\frac{3}{2}} c^{\frac{(9-p_r)}{4}} t^{\frac{(3+p_r)}{4}} \frac{d_{ur}}{c}} & s = 2 \text{ } ct_{dur} \\ \frac{0.03(1.1 \times 10^{18})^{\frac{(1-p_r)}{2}} n_0^{\frac{(p_r+1)}{4}} \Gamma_0^{p_r} E_{52} m_p^{\frac{(5p_r-7)}{4}}}{m_e^{\frac{(3p_r-5)}{2}} \pi^{\frac{(5+p_r)}{4}} q^{\frac{(3-p_r)}{2}} c} & s = 0 \text{ } \frac{R}{2\Gamma_0^2} \\ \frac{4.06(7.7 \times 10^{16})^{\frac{(1-p_r)}{2}} c^{p_r} A_*^{\frac{3(1+p_r)}{4}} \Gamma_0^{1+2p_r} m_p^{\frac{(7p_r-5)}{4}}}{m_e^{\frac{(3p_r-5)}{2}} \pi^{\frac{(3-p_r)}{4}} q^{\frac{(3-p_r)}{2}} E_{52}^{\frac{(p_r-1)}{2}}} & s = 2 \text{ } \frac{R}{2\Gamma_0^2} \end{array} \right. \quad (A1)$$